

Article

Morphology Evolution of Mg₂SiO₄ Particles Synthesized by Spray Pyrolysis from Precursor Solution

Temesgen Yiber Animut ¹, Henni Setia Ningsih ¹ , Wen-Ling Yeh ^{2,3,4,*} and Shao-Ju Shih ^{1,5,*} 

¹ Department of Materials Science and Engineering, National Taiwan University of Science and Technology, No. 43, Sec. 4, Keelung Road, Taipei 10607, Taiwan; d10804828@mail.ntust.edu.tw (T.Y.A.)

² Department of Orthopedic, Lotung Poh-Ai Hospital, No. 81, Nanchang Road, Yilan 26546, Taiwan

³ Department of Medicine, Chang Gung University, No. 259, Wenhua 1st Road, Taoyuan 33302, Taiwan

⁴ Department of Orthopedic, Linkou Chang Gung Memorial Hospital, No. 5, Fuxing Road, Taoyuan 33373, Taiwan

⁵ Department of Fragrance and Cosmetic Science, Kaohsiung Medical University, No. 100, Shih-Chuan 1st Road, Kaohsiung 80708, Taiwan

* Correspondence: pelewly@cgmh.org.tw (W.-L.Y.); shao-ju.shih@mail.ntust.edu.tw (S.-J.S.); Tel.: +886-3-9543131 (ext. 5421) (W.-L.Y.); +886-2-27303716 (S.-J.S.)

Abstract: Forsterite (Mg₂SiO₄) materials have been used in the industrial applications of refractory materials, bone grafting materials, and microwave dielectric materials. In order to avoid the formation of the secondary phase of MgO or MgSiO₃, spray pyrolysis with the precursors of magnesium nitrate hydrate and tetraethyl orthosilicate has been applied to synthesized Mg₂SiO₄ powders. In this study, three typical morphologies of smooth solid sphere, rough hollow sphere, and concaved hollow sphere were observed using scanning electron microscopy and transmission electron microscopy. The experimental results suggested that morphology and particle size distribution are strongly influenced by the calcination temperature. Finally, the corresponding powder formation mechanisms were proposed and discussed.

Keywords: morphology; Mg₂SiO₄; spray pyrolysis; transmission electron microscopy



Citation: Animut, T.Y.; Ningsih, H.S.; Yeh, W.-L.; Shih, S.-J. Morphology Evolution of Mg₂SiO₄ Particles Synthesized by Spray Pyrolysis from Precursor Solution. *Crystals* **2023**, *13*, 639. <https://doi.org/10.3390/cryst13040639>

Academic Editors: Fedlu Kedir Sabir, Osman Ahmed Zelekew, Bedasa Abdisa Gonfa, Lemma Teshome Tufa, Noto Susanto Gultom and Andebet Gedamu Tamirat

Received: 18 March 2023

Revised: 3 April 2023

Accepted: 6 April 2023

Published: 8 April 2023



Copyright: © 2023 by the authors. Licensee MDPI, Basel, Switzerland. This article is an open access article distributed under the terms and conditions of the Creative Commons Attribution (CC BY) license (<https://creativecommons.org/licenses/by/4.0/>).

1. Introduction

Forsterite (Mg₂SiO₄), with an orthorhombic structure, is a well-known stable phase existing in the MgO-SiO₂ system [1]. Mg₂SiO₄-based materials offer the merits of cheapness, easy production, and high stability [2], and these materials have been widely used in many fields of industry. For instance, Mg₂SiO₄ materials have the attractive characteristics of a high melting point of 1890 °C, good insulation properties, and low thermal expansion [3] to be applied as the refractory materials [4]. Due to the advantages of good biocompatibility [2] and high corrosion resistance [5], Mg₂SiO₄ materials have become one of the potential candidates for biocompatible bone graft materials [6]. Moreover, Mg₂SiO₄ materials offer the superior properties of high quality factor and low dielectric constant and play an important role as the microwave dielectric materials in the field of wireless communications [7]. In addition, Mg₂SiO₄ has been used in matrix materials for phosphors owing to its complex crystal structure and the wide absorption and excitation band [8]. Therefore, based on the above applications, extensive studies of Mg₂SiO₄ synthesis have been conducted during the last twenty years, demonstrating the urgent need for Mg₂SiO₄ materials.

Due to the importance of Mg₂SiO₄ powders, many methods have been used for their preparation, including the solid-state method [9,10], the sol-gel method [2,11,12], mechanochemical synthesis [13], the spray drying method [14], and the spray pyrolysis method [15]. Although many synthesis methods were proposed, the main problem of phase segregation still existed. This phase segregation problem has negative effects on the applications of Mg₂SiO₄. For example, Song and Chen [9] reported that the secondary phase

(e.g., MgSiO₃ or MgO phase) decreases the temperature coefficient of the resonant frequency and the quality factor for Mg₂SiO₄, which must be avoided in microwave dielectrics for wireless communications. The possible reasons of phase segregation caused by the various powder synthesis methods are discussed below. First, for the common solid-state method, high-purity raw powders of MgO and SiO₂ are heated up to 1525 °C to form the phase of Mg₂SiO₄; however, the strong water absorption ability of MgO powder compared to that of SiO₂ powder causes the non-stoichiometric compound to generate the undesired secondary phase of MgSiO₃ and MgO [16]. Second, although the sol–gel method provides a molecular level of mixing and high degree of homogeneity compared to the solid-state method, the different hydrolysis and condensation rates of alkoxides and silica may cause the chemical inhomogeneity of the gels to lead to the unwanted secondary phase [17]. Douy [14] used magnesium nitrate and tetraethyl orthosilicate as the Mg and Si precursors to synthesize pure Mg₂SiO₄ via the spray drying method. The spray pyrolysis method was chosen in this study because of its advantages of simply operation and continuous processing [18]. Thus, in order to inhibit the formation of the secondary phase, the similar precursors of magnesium nitrate hydrate and tetraethyl orthosilicate were chosen to fabricate Mg₂SiO₄ using spray pyrolysis.

In this study, spray-pyrolyzed Mg₂SiO₄ powders calcined at a series of temperatures from 850 to 1000 °C were prepared. Then, the phase compositions, surface morphologies, inner structures, specific surface areas, and chemical compositions were examined using X-ray diffraction (XRD), a scanning electron microscope (SEM), a transmission electron microscope (TEM), nitrogen/desorption isotherm, and X-ray energy-dispersive spectroscopy (XEDS), respectively. In addition, by combining the SEM and TEM observations, various morphologies were identified for each Mg₂SiO₄ powder, and the corresponding fractions were obtained to correlate with the calcination temperature. Finally, the formation mechanisms of distinct morphological Mg₂SiO₄ particles were proposed and discussed.

2. Materials and Methods

2.1. Fabrication of Mg₂SiO₄ Powder

The Mg₂SiO₄ powders were synthesized using spray pyrolysis technique with the molar ratio Mg:Si = 2:1. Initially, to prepare the precursor solution, 27.3 g of tetraethyl orthosilicate (Si(OC₂H₅)₄, 98.0%, Thermo scientific, Waltham, MA USA) and 68.3 g magnesium nitrate hydrate (Mg(NO₃)₂·6H₂O, 99.0%, Acros organics, Geel, Belgium) were dissolved in 1000 mL of deionized (DI) water. Then, 27 mL of 2M nitric acid (HNO₃, 69.5%, Scharlau, Barcelona, Spain) was added as an acid medium; this precursor solution was stirred for 2 h at room temperature to obtain a homogenous solution. For the spray pyrolysis, the obtained precursor solution was transferred into an ultrasonic nebulizer (KT-100A, King Ultrasonic, New Taipei, Taiwan) with a frequency 1.6 MHz in order to generate precursor droplets. Subsequently, these droplets were contained in a quartz tube and heated in a furnace (D110, Denying, New Taipei, Taiwan) with three zones of preheating (350 °C), calcinating (850, 900, 950, or 1000 °C), and cooling (450 °C). Finally, the resulting spray-pyrolyzed powders were collected.

2.2. Characterization of Mg₂SiO₄ Powder

The phase compositions and the related crystalline sizes of Mg₂SiO₄ powders were analyzed using an X-ray diffractometer (XRD) (D2 Phaser, Bruker, Berlin, Germany) with Ni-filtered Cu K α radiation ($\lambda = 1.5405 \text{ \AA}$). The samples were scanned between the 2θ from 20° to 80° with the scan step of 0.05° and the speed of 5° min⁻¹ to obtain their phase compositions; the crystalline size (D) of each powder was acquired from the three most intense peaks out of the diffraction peaks using Scherrer's equation, and the equation is given below.

$$D = \frac{k\lambda}{\beta_{hkl}\cos\theta} \quad (1)$$

where D is crystallite size, k is shape factor of 0.9, λ is wavelength of Cu $K\alpha$ radiation, β_{hkl} is the line broadening at half the maximum intensity at 2θ , and θ is the Bragg angle.

Next, for the surface morphologies, the Mg_2SiO_4 powders were observed using a field-emission scanning electron microscope (FE-SEM) (JSM 6500F, JEOL, Tokyo, Japan). The FE-SEM analysis was performed under high vacuum with energy 10 kV and working distance of 10 mm. Before observation, the specimens were platinum sputter-coated for 30 s at a current of 10 mA. Moreover, a transmission electron microscope (TEM) (Tecnai G2 F20, FEI, Hillsboro, OR, USA) was employed to investigate the inner morphologies of Mg_2SiO_4 powders. The TEM samples were prepared by sonicating a small amount of Mg_2SiO_4 powders with acetone and dropped onto a 300-mesh Cu grid. The particle size distributions of Mg_2SiO_4 powders were obtained by measuring the diameter of 300 randomly selected particles from the SEM images. The specific surface areas were measured by applying N_2 adsorption–desorption analysis (Autosorb-1, Quantachrome Instruments, Boynton Beach, FL, USA). Prior to measurement, the specimens were degassed under vacuum at 200 °C for 3 h. Finally, the chemical compositions of Mg_2SiO_4 powders were evaluated by energy dispersive X-ray spectrometry (XEDS) (INCA, Oxford Instruments, Oxford, UK), and over 15 particles were examined to acquire the precise concentrations.

3. Results

The phase compositions of various calcined Mg_2SiO_4 powders were obtained using XRD as shown in Figure 1, and the JCPDF spectra of Mg_2SiO_4 and MgO are inserted in the bottom of the figure; from the figure it can be seen that the 850 °C calcined powder contained the main phase of the Mg_2SiO_4 phase (JCPDS number 34-0189) and the secondary phase of MgO (JCPDS number 75-1525), and similar XRD patterns were obtained for the 900 and 950 °C calcined powders. On the other hand, the 1000 °C calcined powder exhibited the single phase of Mg_2SiO_4 . To the eye, the intensities of the Mg_2SiO_4 diffraction peaks increase with the increasing calcination temperature, which suggests the calcination temperature enhances the crystallinity of Mg_2SiO_4 . In addition, there was no obvious shift of the main diffraction peaks for all calcined powders, which suggests there is no obvious variation in the lattice parameters. Based on Scherrer's equation, the average crystalline size and standard deviation of the 850, 900, 950, and 1000 °C calcined powders were 30.0 ± 1.7 , 31.6 ± 1.8 , 35.4 ± 1.9 , and 43.5 ± 2.1 nm, respectively. The crystallite measurements (Scherrer's equation) showed that the powder with the higher calcined temperature exhibited the higher crystallinity (larger peak intensity) and the larger Mg_2SiO_4 crystalline size (e.g., 43.5 ± 2.1 nm in the 1000 °C case compared to 30.0 ± 1.7 nm in the 850 °C case). In short, all XRD spectra showed that the powder calcined at the temperature of 1000 °C exhibited the single phase, which suggests the Mg_2SiO_4 powders were synthesized successfully using spray pyrolysis.

Figure 2 shows SEM images of the typical Mg_2SiO_4 powders calcined at temperatures of 850, 900, 950, and 1000 °C. As shown in Figure 2a, the 850 °C calcined powder exhibited the three surface morphologies of smooth sphere, rough sphere, and concaved sphere. The same surface morphologies were also obtained for the other Mg_2SiO_4 powders (see Figure 2b–d). Furthermore, the relationship between particle morphology and its particle size was determined using the SEM micrographs. For Mg_2SiO_4 powders, the particle sizes of smooth sphere, rough sphere, and concaved sphere ranged from 713 ± 158 , 836 ± 241 , and 688 ± 181 nm, respectively; the order of particle size for the three typical morphologies was rough sphere > smooth sphere > concaved sphere. On the other hand, Figure 3 represents the particle size distribution histograms of 850, 900, 950, and 1000 °C calcined Mg_2SiO_4 powders; all powders show a normal distribution. Based on the statistical analysis, the particle sizes of 850, 900, 950, and 1000 °C calcined powders were 744.4 ± 351.9 , 865.2 ± 284.0 , 886.8 ± 307.7 , and 938.6 ± 358.1 nm, respectively; the result revealed that the higher calcination powder had the larger particle size (e.g., 938.6 ± 358.1 nm in the 1000 °C case but 744.4 ± 351.9 nm in the 850 °C case). In summary, three typical surface morphologies of smooth sphere, rough sphere, and concaved sphere were detected, and

the concaved sphere had the largest particle size when compared to the smooth sphere and rough sphere. A direct relationship between particle size and calcination temperature was also inferred from the statistical data.

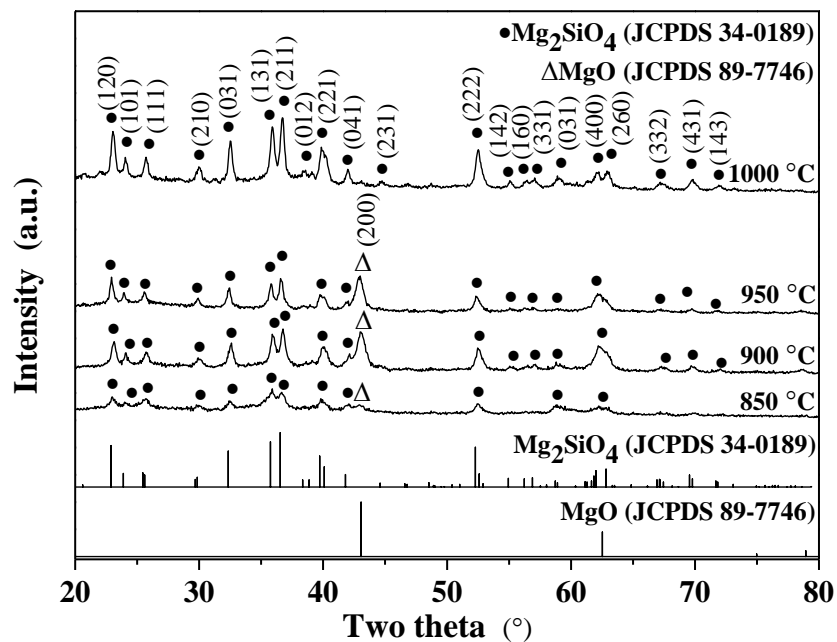


Figure 1. XRD patterns of Mg_2SiO_4 -calcined powders at temperatures of 850, 900, 950, and 1000 °C.

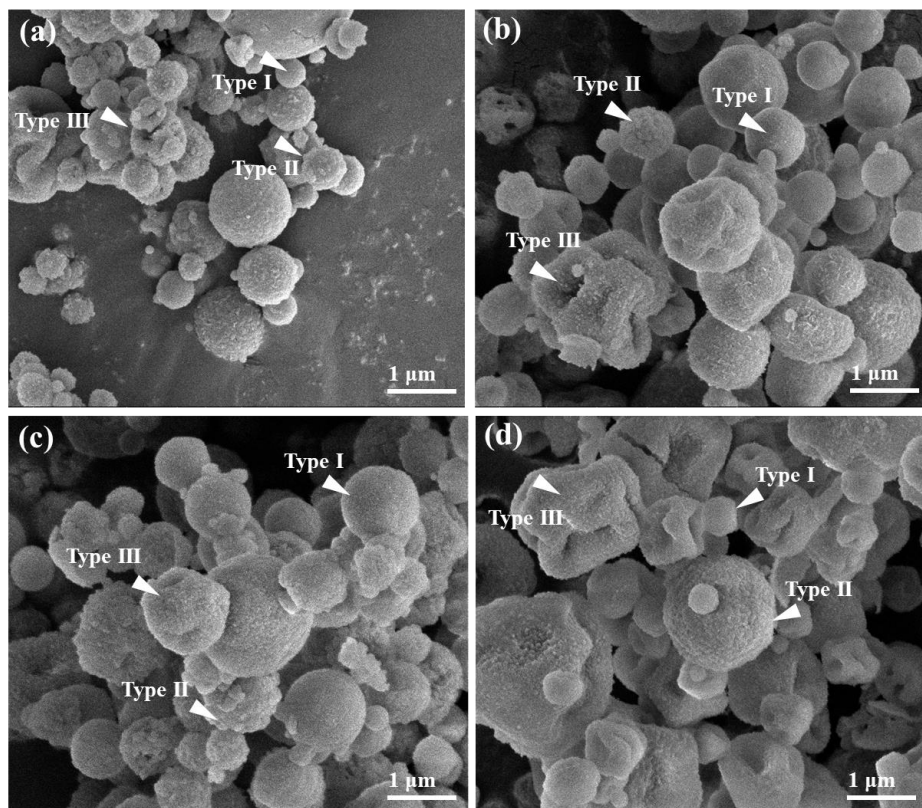


Figure 2. SEM micrographs of Mg_2SiO_4 -calcined powders at (a) 850, (b) 900, (c) 950, and (d) 1000 °C. The various morphological types are highlighted with triangles.

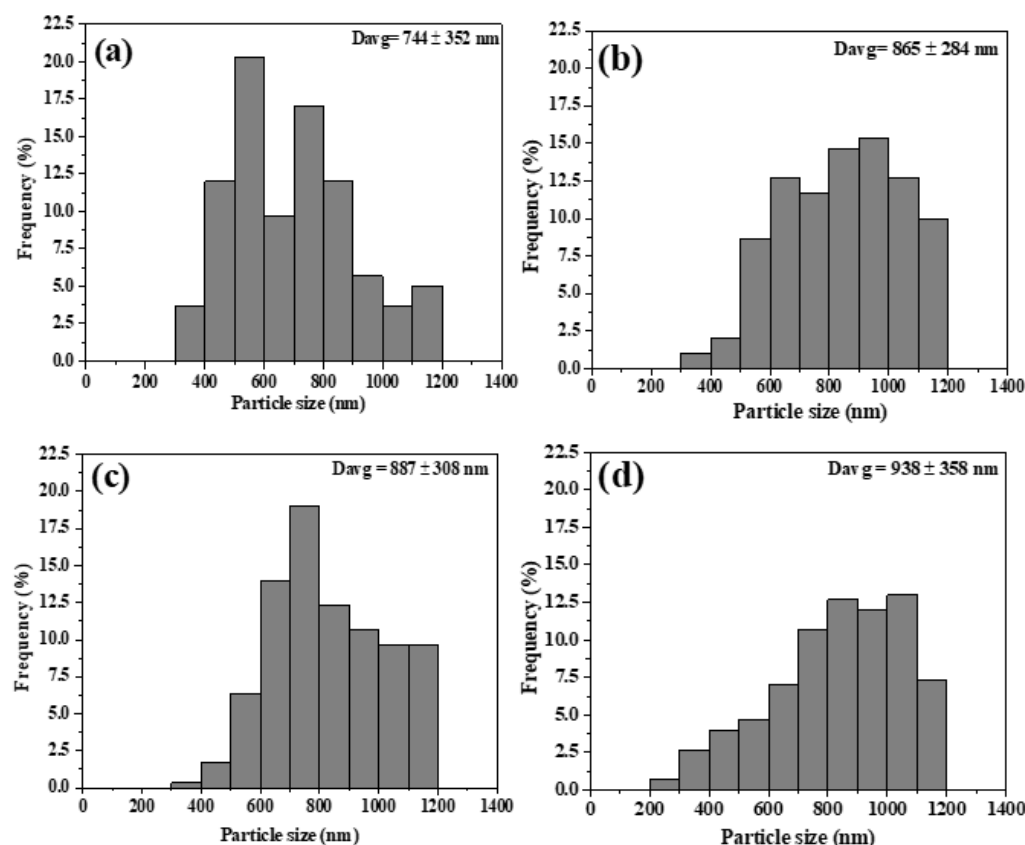


Figure 3. Particle size distributions of Mg_2SiO_4 -calcined powders at temperatures of (a) 850, (b) 900, (c) 950, and (d) 1000 °C.

Figure 4 shows the TEM images of all Mg_2SiO_4 powders. It should be noted that it is not easy to distinguish open and closed pores from the particles in the two-dimensional TEM projection images; therefore, the surface morphology from SEM images (Figure 2) and the inner structure from TEM observations (Figure 4) are required to obtain the three-dimensional morphologies of typical Mg_2SiO_4 powders. So, Figure 4a reveals the three main morphologies of smooth solid sphere (Type I), rough hollow sphere (Type II), and concaved hollow sphere (Type III) in the 850 °C calcined Mg_2SiO_4 powder; also, similar Types I, II, and III particles were observed in the TEM micrographs, as revealed in Figure 4b–d.

Moreover, the populations of three typical morphologies from four Mg_2SiO_4 powders were measured statistically, as shown in Figure 5: the 850 °C calcined powder had 89.2% Type I, 10.0% Type II, and 0.8% Type III particles; the 900 °C calcined powder had 85.0% Type I, 14.1% Type II, and 0.9% Type III particles; the 950 °C calcined powder had 3.4% Type I, 65.0% Type II, and 31.6% Type III particles; and the 1000 °C calcined powder had 4.5% Type I, 10.0% Type II, and 85.5% Type III particles. From the figure, a higher population of Type I particles is observed in the cases of 850 and 900 °C (89.2% for 850 °C and 85.0% for 900 °C), but the highest populations of the 950 and 1000 °C calcined powders are Type II and Type III, respectively. The result suggests that the calcination temperature controls the particle morphology and the related population for the spray-pyrolyzed Mg_2SiO_4 powders.

Figure 6 shows the nitrogen adsorption/desorption isotherms and their pore size distributions of 850, 900, 950, and 1000 °C calcined Mg_2SiO_4 powders. Based on the original IUPAC classification, all BET isotherms were identified as Type H4 loop [19], which indicates that all powders contain mesopores; from the pore size measurements, all powders are mesoporous with the pore size less than 18 nm.

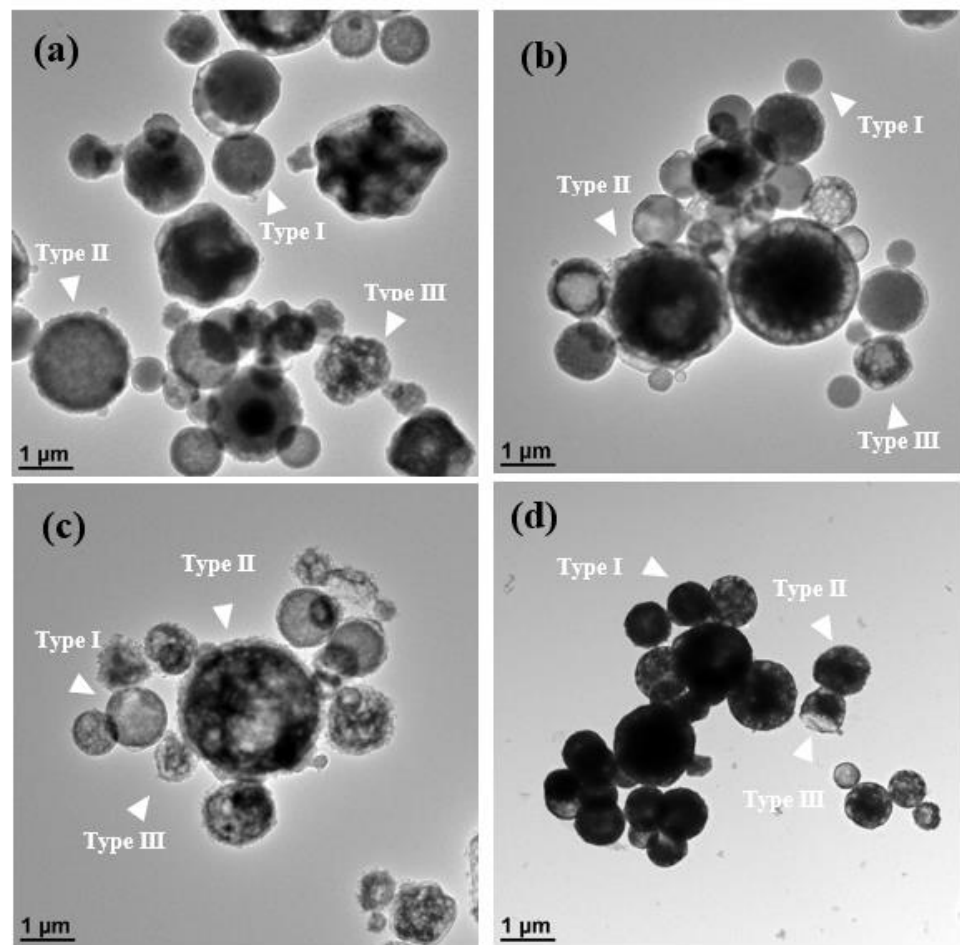


Figure 4. TEM images of Mg_2SiO_4 -calcined powders at (a) 850, (b) 900, (c) 950, and (d) 1000 °C. The various morphological types are highlighted with triangles.

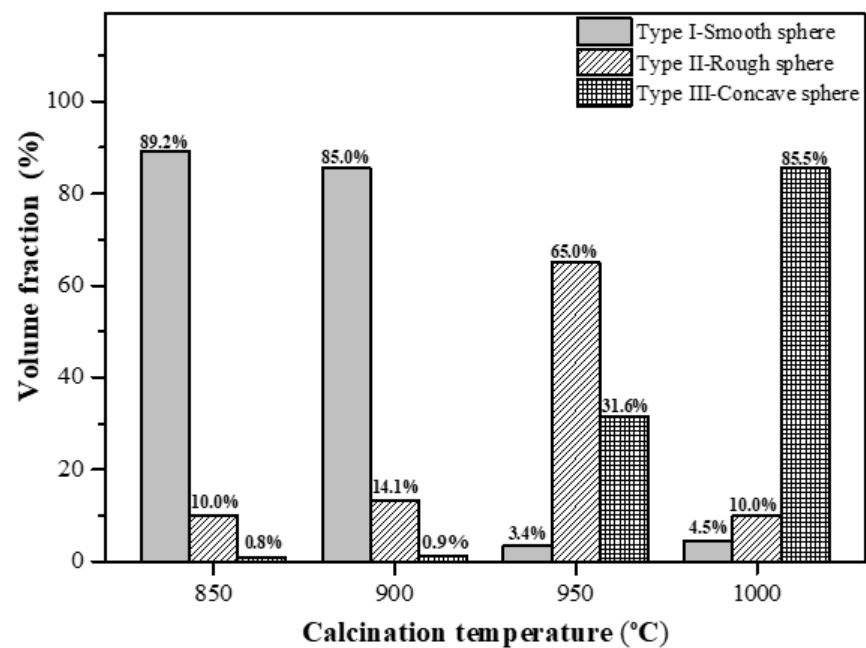


Figure 5. Morphology distributions of Mg_2SiO_4 powders calcined at temperatures of 850, 900, 950, and 1000 °C.

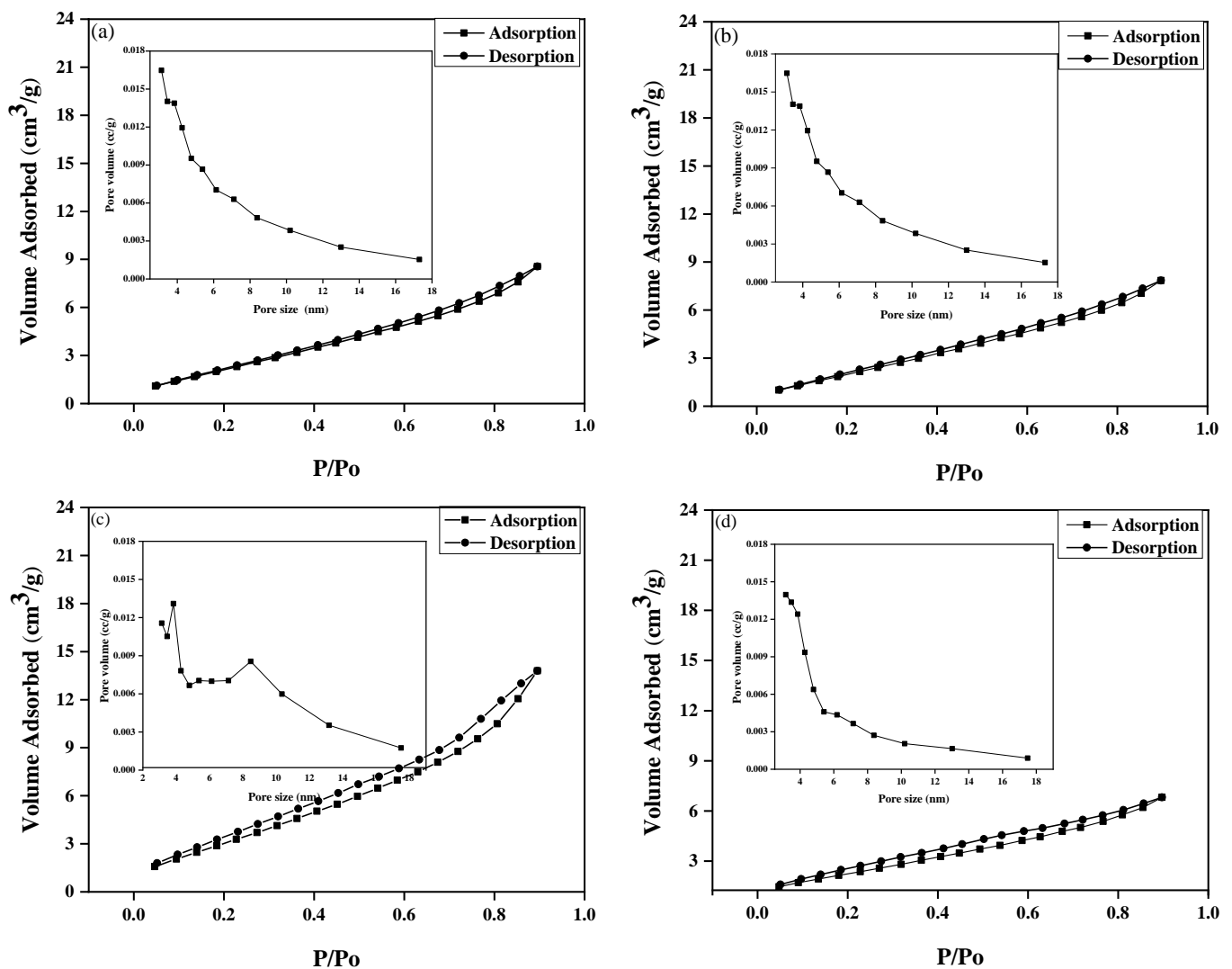


Figure 6. Adsorption and desorption curves of Mg_2SiO_4 powders calcined at the temperatures of (a) 850, (b) 900, (c) 950, and (d) 1000 °C. The inserts are their corresponding pore size distributions.

Additionally, the BET measurements indicated the specific surface areas of 16.3 ± 4.0 , 18.9 ± 5.4 , 21.4 ± 5.1 , and 16.8 ± 5.1 m^2/g for 850, 900, 950, and 1000 °C calcined powders, respectively. From the data, the specific surface area increased with the calcination temperature from 850 to 950 °C, but the value of the specific surface area declined rapidly at the temperature of 1000 °C.

Figure 7 indicates the typical XEDS spectra of the Mg_2SiO_4 powders calcined from 850 to 1000 °C; C-K α and Pt-M α peaks were obtained from the environment and surface conductive coating (to avoid sample charging), respectively; the main XEDS peaks of O-K α (0.53 keV), Mg-K α (1.25 keV), and Si-K α (1.74 keV) suggest that Mg_2SiO_4 powders contained O, Mg, and Si elements. Furthermore, the 850 °C calcined powder yielded $21.59 \pm 0.67\%$ Mg and $10.43 \pm 0.45\%$ Si. Similar results were acquired for the 900, 950, and 1000 °C calcined Mg_2SiO_4 powders ($21.28 \pm 1.41\%$ Mg and $10.14 \pm 1.15\%$ Si in the 900 °C case, $21.58 \pm 0.69\%$ Mg and $10.09 \pm 1.28\%$ Si in the 950 °C case, and $20.01 \pm 0.86\%$ Mg and $10.62 \pm 1.87\%$ Si in the 1000 °C case). It should be noted that no oxygen information is provided because the energy of O-K α is too low to be identified precisely using XEDS.

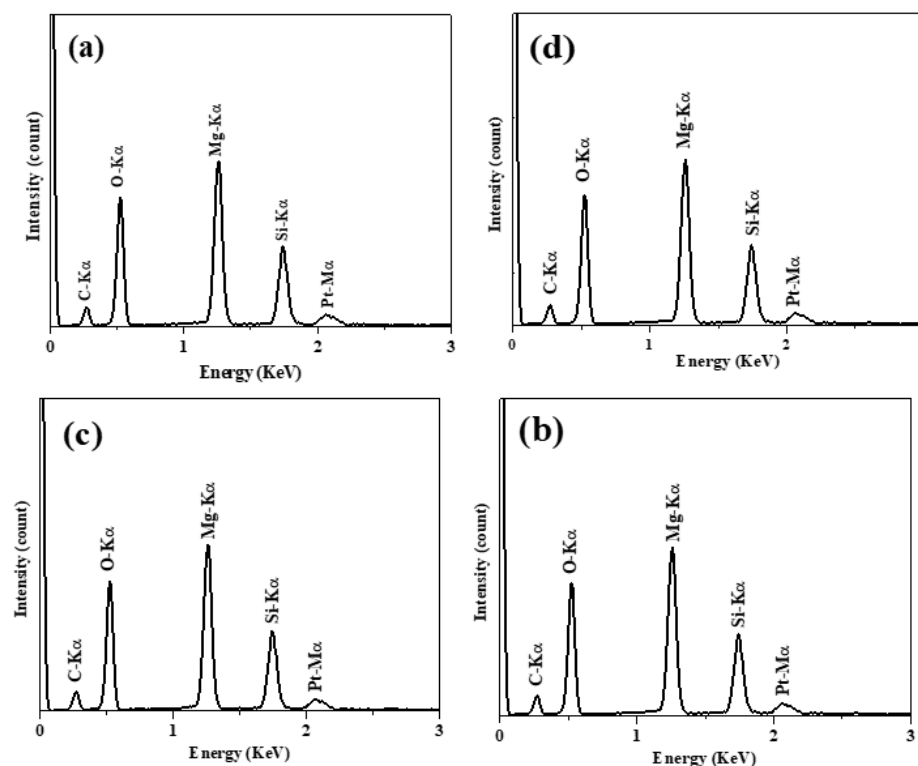


Figure 7. XEDS spectra of Mg_2SiO_4 powders calcined at the temperatures of (a) 850, (b) 900, (c) 950, and (d) 1000 °C.

4. Discussion

Regarding the phase composition issue, Douy [14] investigated spray-dried Mg_2SiO_4 powders with various temperatures from 250 to 1500 °C, and in that study, weak diffraction peaks of MgO and Mg_2SiO_4 phases were detected at the temperature of 500 °C and stronger diffraction peaks of Mg_2SiO_4 were observed at 700 °C; then, after heating to 1200 °C, the pure Mg_2SiO_4 phase was characterized due to the complete reaction between amorphous SiO_2 and crystalline MgO. Unlike the Mg_2SiO_4 powders prepared from the solid-state method [9], no second phase of MgO or MgSiO_3 was obtained in the 1000 °C calcined Mg_2SiO_4 powders. This result may be attributed to that the liquid mixture of the spray pyrolysis method is more homogenous than the solid mixture of the solid-state method to minimize the effect of a diffusion coefficient difference between Mg^{2+} and Si^{4+} . According to the Mg_2SiO_4 synthesis model of the solid-state method proposed by Gardés et al. [20], the diffusion coefficient of Mg^{2+} is much faster than that of Si^{4+} , and therefore the diffusion reaction is determined by Mg^{2+} . During the calcination process, Mg^{2+} diffuses from MgO to the surface of SiO_2 to form the phase of MgSiO_3 . Then, more Mg^{2+} moves to surface of MgSiO_3 to form the phase of Mg_2SiO_4 [20]. Thus, due to the different diffusion coefficients between Mg^{2+} and Si^{4+} , the secondary phases of MgO and MgSiO_3 are detected easily in the solid-state method. On the other hand, from the XRD patterns (Figure 1), the 1000 °C calcined powder exhibited more diffraction peaks of Mg_2SiO_4 than that of 950, 900, and 850 °C calcined powders; also, the crystalline size increased with the calcination temperature (43.5 ± 2.1 nm for 1000 °C calcined powder and 30.0 ± 1.7 nm for 850 °C calcined powder). Both results suggest the higher calcination temperature, the higher crystallinity for the spray-pyrolyzed Mg_2SiO_4 powders.

Our SEM and TEM micrographs clearly identified three typical morphologies, namely smooth solid sphere (Type I), rough hollow sphere (Type II), and concaved hollow sphere (Type III) (see Figures 2 and 4); the three proposed morphological mechanisms for the various calcinated Mg_2SiO_4 powders (temperature from 850 to 1000 °C) via three stages of solvent evaporation, solute decomposition, and particle calcination are plotted in Figure 8.

For spray pyrolysis, “one-particle-per-drop” and “gas-to-particle conversion” are the two main mechanisms [18]. “One-particle-per-drop” represents that the characteristics of a particle (e.g., size or morphology) are directly related to the precursor droplets; on the other hand, “gas-to-particle conversion” represents that the particles are deposited from the homogenous gas phase, and these particles are normally in the nanometer size range [18]. In this study, among these three morphological particles, no nanosized particle was observed from the size measurements, which indicates the dominate SP formation mechanism of Mg_2SiO_4 powders is “one-particle-per-drop”, not “gas-to-particle conversion” [18]. Therefore, Figure 8 represents the mechanisms of these three morphological Mg_2SiO_4 powders from precursor droplets to calcined particles based on the “one-particle-per-drop” mechanism. For this mechanism, it is noted that the two precipitation phenomena of “volume precipitation” and “surface precipitation” determine the morphology of spray-pyrolyzed particles [18]. In our study, the solute of smaller droplets precipitated homogeneously (the solute precipitates with the similar speed through the surface and center of the droplet, called volume precipitation phenomenon) to form smooth solid sphere (Type I) [18]; whereas, the solute of larger droplets precipitated inhomogeneous (the solute precipitates faster in the surface than the center of the particle, called surface precipitation phenomenon) to form the hollow particles [21], including rough hollow sphere (Type II) and concaved hollow sphere (Type III), in this study. Furthermore, among the hollow particles (generated from surface precipitation phenomenon), a discussion of the difference between the concaved hollow shape of Type III and rough hollow shape of Type II follows. The larger droplets form the hollow particle and then receive a larger deformation force inducing fracture for concaved hollow sphere (Type III), whereas the hollow structure from smaller droplets receives the smaller deformation force, and this force is too weak to induce fracture [21]. In summary, the higher calcination temperature induced a larger deformation force during the cooling stage to form more fractures, and therefore more concaved hollow sphere particles were obtained (85.5% of Type III particles for 1000 °C); also, the lower calcination temperature induced a smaller deformation force, and more rough hollow sphere particles were observed (65.0% of Type II particles for 950 °C).

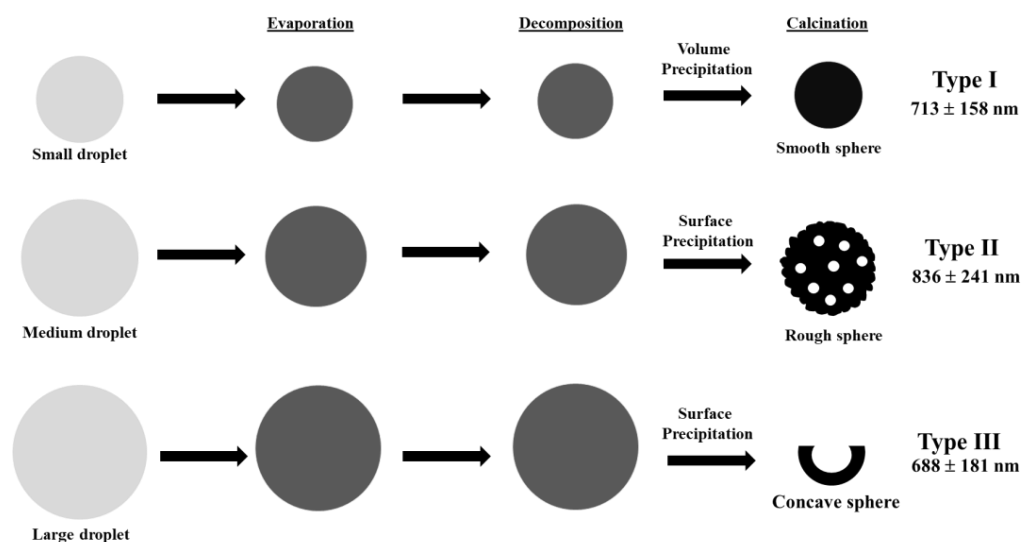


Figure 8. Schematic diagram illustrating the formation mechanism of the main particle morphology of Mg_2SiO_4 powders for SP stages.

Also, from our data, it is clear that there is a strong relationship between particle size and particle morphology. To begin with, the Mg_2SiO_4 powders from this study were formed by the “one-particle-per-drop” mechanism [18], which suggests that the particle size is controlled by the precursor droplet. The concentration of precursor was the same for each Mg_2SiO_4 powder, and the particles (from the same-sized precursor droplets) had the

same mass. So, the particle included more pores resulting in the larger particle size. In this study, the Type II particles had more porosity than Type I particles, and therefore, Type II particles (836 nm) exhibited the larger particle size than that of Type I particles (713 nm). A similar result has been reported in our previous study [22].

Figure 5 presents the population of Mg_2SiO_4 particles as a function of morphological type; the lower calcination temperature cases (850 °C and 900 °C) contained more of solid shape (Type I), whereas the higher calcination temperature cases (950 °C and 1000 °C) contained more of porous shape (Type II or III). The reason the higher calcination temperature results in a more porous structure is described below. Since the droplet-size-controlling factors of precursor concentration and ultrasonic frequency was kept the same, the droplet size was the same for the four calcined Mg_2SiO_4 powders. Since the length of tube furnace was the same, the cooling rate of higher calcination temperature was larger than that of the lower calcination temperature. The faster cooling rate case causes the larger deformation force to form more porous structural particles (Type II or III) comparing to the slower cooling rate case (lower deformation force for the solid structural particles). Based on our SEM and TEM observations, various morphological particles have their own particle sizes (e.g., 713 nm for Type I, 836 nm for Type II, and 688 nm for Type III). Thus, the calcination factor of spray pyrolysis controls the particle morphology and then influences the particle size.

On the other hand, when combining BET data and morphology distribution (Figure 5), the powder with the higher Type II population (lower Type I population) results in the larger specific surface area. For example, the 850 °C calcined powder (89.2 Type I and 10.0% Type II particles) exhibited the small specific surface area of $16.3 \pm 4.0 \text{ m}^2/\text{g}$, whereas the 950 °C calcined powder (3.4% Type I and 65.0 Type II particles) exhibited the larger specific surface area of $21.4 \pm 5.1 \text{ m}^2/\text{g}$. This result shows that morphology distribution does affect the specific surface area of Mg_2SiO_4 particles.

Considering chemical composition, the Mg/Si ratio is 2.0. The XEDS data suggested that the Mg/Si ratios of 850, 900, 950, and 1000 °C calcined powders were 2.1 ± 0.7 , 1.9 ± 0.3 , 1.8 ± 0.2 , and 2.1 ± 1.0 , respectively, which is very close to the theoretical ratio of 2. This result implies that the main Mg_2SiO_4 phase was obtained after calcination in the temperature range of 850 to 1000 °C.

5. Conclusions

Using spray pyrolysis, pure Mg_2SiO_4 powders were synthesized successfully under various calcination temperatures from 850 to 1000 °C. XEDS data also confirmed that the Mg/Si ratio of 1000 °C calcined powder was very close to the theoretical ratio of 2, which revealed that no phase segregation was detected. In addition, Mg_2SiO_4 particles were of three main morphologies: smooth solid sphere, rough hollow sphere, and concaved hollow sphere. According to the statistical analysis, the calcination temperature condition controlled the particle morphology and the related population of the powders. The relationship between morphology and particle size was also investigated. Finally, the corresponding formation mechanisms of these three typical particles was discussed.

Author Contributions: Conceptualization, S.-J.S.; methodology, T.Y.A.; validation, S.-J.S., W.-L.Y. and H.S.N.; formal analysis, T.Y.A. and H.S.N.; investigation, T.Y.A.; data curation, T.Y.A.; writing—original draft preparation, S.-J.S.; writing—review and editing, S.-J.S. and H.S.N.; supervision, S.-J.S.; project administration, S.-J.S.; funding acquisition, W.-L.Y. All authors have read and agreed to the published version of the manuscript.

Funding: Lo-Hsu Medical Foundation, Lotung Poh-Ai Hospital. This research was supported by a grant from the Lo-Hus Medical Foundation, Inc. Lotung Poh-Ai Hospital *Number: E187.

Institutional Review Board Statement: Not applicable.

Informed Consent Statement: Not applicable.

Data Availability Statement: The data that support the findings of this study are available from the corresponding author upon reasonable request.

Acknowledgments: We acknowledge funding from the Taiwan National Science and Technology Council (grant number NSTC 108-2923-E-011-007-MY3), Taipei Medical University/National Taiwan University of Science and Technology cross-university collaboration project (grant number of TMU-NTUST-111-10), and Lotung Poh-Ai Hospital (grant number of 11106).

Conflicts of Interest: The authors declare no conflict of interest.

References

1. McDonnell, R.; Spiers, C.; Peach, C. Fabrication of dense forsterite–enstatite polycrystals for experimental studies. *Phys. Chem. Miner.* **2002**, *29*, 19–31. [\[CrossRef\]](#)
2. Ni, S.; Chou, L.; Chang, J. Preparation and characterization of forsterite (Mg_2SiO_4) bioceramics. *Ceram. Int.* **2007**, *33*, 83–88. [\[CrossRef\]](#)
3. Ramezani, A.; Emami, S.; Nemat, S. Effect of waste serpentine on the properties of basic insulating refractories. *Ceram. Int.* **2018**, *44*, 9269–9275. [\[CrossRef\]](#)
4. Hossain, S.S.; Mathur, L.; Singh, P.; Majhi, M.R. Preparation of forsterite refractory using highly abundant amorphous rice husk silica for thermal insulation. *J. Asian Ceram. Soc.* **2017**, *5*, 82–87. [\[CrossRef\]](#)
5. Kazemi, C.; Bemani, A.; Alizadeh, M.; Siyahati, G.; Ardakani, T. Environmental sustainability assessment of Nile tilapia (*Oreochromis niloticus*) breeding in biofloc system. *Iran. J. Fish. Sci.* **2022**, *21*, 1508–1526.
6. Mirhadi, S. Synthesis and characterization of nanostructured forsterite scaffolds using two step sintering method. *J. Alloys Compd.* **2014**, *610*, 399–401. [\[CrossRef\]](#)
7. Ohsato, H.; Tsunooka, T.; Sugiyama, T.; Kakimoto, K.-I.; Ogawa, H. Forsterite ceramics for millimeterwave dielectrics. *J. Electroceramics* **2006**, *17*, 445–450. [\[CrossRef\]](#)
8. Liu, Y.; Liu, Y.; Huang, X.; Wu, M.; He, C.; Liu, Q.; Min, X.; Huang, Z.; Mi, R.; Wang, H. Synthesis and photoluminescence properties of Eu^{2+} -doped olivine Mg_2SiO_4 blue-emitting phosphor for plant growth. *J. Mater. Sci. Mater. Electron.* **2023**, *34*, 209. [\[CrossRef\]](#)
9. Song, K.; Chen, X. Phase evolution and microwave dielectric characteristics of Ti-substituted Mg_2SiO_4 forsterite ceramics. *Mater. Lett.* **2008**, *62*, 520–522. [\[CrossRef\]](#)
10. Zhao, F.; Zhang, L.; Ren, Z.; Gao, J.; Chen, X.; Liu, X.; Ge, T. A novel and green preparation of porous forsterite ceramics with excellent thermal isolation properties. *Ceram. Int.* **2019**, *45*, 2953–2961. [\[CrossRef\]](#)
11. Belyakov, A.; Andrianov, N.; Strel'nikova, S. Evaluation of the magnesium and silicon diffusion rates in forsterite synthesis using various magnesium compounds. *Inorg. Mater.* **2012**, *48*, 176–180. [\[CrossRef\]](#)
12. Tamin, S.; Adnan, S.B.R.S.; Jaafar, M.H.; Mohamed, N.S. Effects of sintering temperature on the structure and electrochemical performance of Mg_2SiO_4 cathode materials. *Ionics* **2018**, *24*, 2665–2671. [\[CrossRef\]](#)
13. Nguyen, P.Q.; McKenzie, W.; Zhang, D.; Xu, J.; Rapp, R.; Bradley, J.P.; Dera, P. Mechanochemical Synthesis of Nanocrystalline Olivine-Type Mg_2SiO_4 and MgCoSiO_4 . *Crystals* **2022**, *12*, 369. [\[CrossRef\]](#)
14. Douy, A. Aqueous syntheses of forsterite (Mg_2SiO_4) and enstatite (MgSiO_3). *J. Sol-Gel Sci. Technol.* **2002**, *24*, 221–228. [\[CrossRef\]](#)
15. Tani, T.; Saeki, S.; Suzuki, T.; Ohishi, Y. Chromium-Doped Forsterite Nanoparticle Synthesis by Flame Spray Pyrolysis. *J. Am. Ceram. Soc.* **2007**, *90*, 805–808. [\[CrossRef\]](#)
16. Fathi, M.; Kharaziha, M. Mechanically activated crystallization of phase pure nanocrystalline forsterite powders. *Mater. Lett.* **2008**, *62*, 4306–4309. [\[CrossRef\]](#)
17. Petričević, V.; Gayen, S.K.; Alfano, R.R.; Yamagishi, K.; Anzai, H.; Yamaguchi, Y. Laser action in chromium-doped forsterite. *Appl. Phys. Lett.* **1988**, *52*, 1040–1042. [\[CrossRef\]](#)
18. Messing, G.; Zhang, S.; Jayanthi, G. Modeling of particle morphology and size. *J. Am. Ceram. Soc.* **1993**, *76*, 2707. [\[CrossRef\]](#)
19. Thommes, M.; Kaneko, K.; Neimark, A.V.; Olivier, J.P.; Rodriguez-Reinoso, F.; Rouquerol, J.; Sing, K.S.W. Physisorption of gases, with special reference to the evaluation of surface area and pore size distribution (IUPAC Technical Report). *Pure Appl. Chem.* **2015**, *87*, 1051–1069. [\[CrossRef\]](#)
20. Gardés, E.; Wunder, B.; Wirth, R.; Heinrich, W. Growth of multilayered polycrystalline reaction rims in the MgO-SiO_2 system, part I: Experiments. *Contrib. Mineral. Petrol.* **2011**, *162*, 37–49. [\[CrossRef\]](#)
21. Shih, S.-J.; Herrero, P.R.; Li, G.; Chen, C.-Y.; Lozano-Perez, S. Characterization of mesoporosity in ceria particles using electron microscopy. *Microsc. Microanal.* **2011**, *17*, 54–60. [\[CrossRef\]](#) [\[PubMed\]](#)
22. Shih, S.J.; Lin, Y.C.; Lin, S.H.; Yu, C.Y. Correlation of morphology and photoluminescence properties of gehlenite: Eu glassy phosphors. *Int. J. Appl. Ceram. Technol.* **2017**, *14*, 56–62. [\[CrossRef\]](#)

Disclaimer/Publisher's Note: The statements, opinions and data contained in all publications are solely those of the individual author(s) and contributor(s) and not of MDPI and/or the editor(s). MDPI and/or the editor(s) disclaim responsibility for any injury to people or property resulting from any ideas, methods, instructions or products referred to in the content.